IEEE Photonics Journal
An IEEE Photonics Society Publication

Open Access

High-Stability Algorithm in White-Light Phase-Shifting Interferometry for Disturbance Suppression

Volume 10, Number 5, September 2018

Chunxi Zhang
Haowei Li
Ningfang Song
Huipeng Li

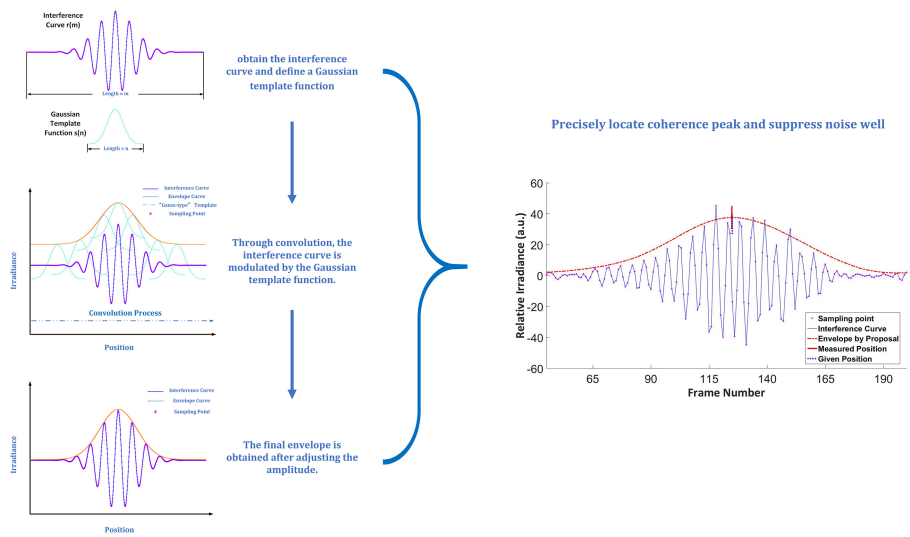

DOI: 10.1109/JPHOT.2018.2867001
1943-0655

High-Stability Algorithm in White-Light Phase-Shifting Interferometry for Disturbance Suppression

Chunxi Zhang, Haowei Li, Ningfang Song, and Huipeng Li

School of Instrumentation Science and Opto-electronics Engineering, Beihang University, Beijing 100191, China

DOI:10.1109/JPHOT.2018.2867001

Manuscript received June 22, 2018; revised July 31, 2018; accepted August 10, 2018. Date of publication August 24, 2018; date of current version September 6, 2018. This work was supported by National Key Scientific Instrument and Equipment Development Project of China under Grant 2013YQ040877.
Corresponding author: Haowei Li (e-mail: f-22l lhwbenz@163.com).

Abstract: A hybrid algorithm, combining a "Gauss-type" envelope algorithm with the Carré algorithm, is proposed for disturbance suppression. For white-light phase-shifting interferometry (WLPSI), this novel algorithm provides suitable performance in suppressing noise caused by external conditions, such as mechanical vibrations, low-reflectivity surfaces, and poor-contrast interferograms. The algorithm is mathematically derived, and simulation testing is performed at the micro level to demonstrate that the algorithm can position the coherence peak correctly under challenging conditions. At the macro level, the algorithm is further verified on standard samples, with the repeatability of the step height being less than 0.32% in a favorable environment and 0.59% in a noisy environment. The repeatability of the roughness was 0.23% in a favorable environment and 0.65% in a noisy environment. Note that "repeatability" = "standard deviation" / "dean value", reflecting the stability as a percentage. The simulated and experimental results prove that the proposed algorithm is highly precise and robust. This algorithm reduces the environmental dependence of the performance of WLPSI instrumentation and expands its range of application.

Index Terms: White-light phase-shifting interferometry, "Gauss-type" envelope, Disturbance suppression.

1. Introduction

Interferometric techniques for shape measurement, such as white-light interferometry (WLI), phase-shifting interferometry (PSI) [1], and their combination (WLPSI), are based on the analysis of the interference pattern of two beams—the object beam reflected from the sample and the reference beam reflected from the reference mirror [2], [3]. When the optical path difference between the object beam and the reference beam is zero, the interference signal takes its maximum value [4], which is called the coherence peak. WLPSI not only has the accuracy of PSI but also exhibits the resolution of WLI. When the position of the coherence peak envelope and the phase information are detected, WLPSI can yield clear height data [4], [5].

The coherence peak detection algorithm lies at the core of WLPSI [6], [7], and the envelope method is the most widely used method for this purpose. Current research typically focuses on generating an accurate envelope [8], [9] and improving the envelope detection and extraction performance. An overview of various methods of creating the envelope is presented in [10].

However, in practical applications, the measurement process is somewhat affected by noise [11]. Reference [8] describes how noise affects the fringe-order determination. References [12], [13] address how noise affects the interferogram envelope. Noise directly changes the shape of the interference curve. If the envelope and phase are calculated from a noisy signal, then these parameters are also affected by the noise [14]. The methods described in [15] provide high measurement efficiency; however, such approaches cause the parameters to become more sensitive to noise, leading to unacceptable inaccuracy in coherence peak detection. As a result, determining how to suppress the influence of noise on the measurement results has become increasingly important.

Zili Lei first used the Hilbert transform (HT) to obtain the envelope and then performed cross-correlation calculations to obtain a series of reference positions, which were averaged to calculate the height [11]. In this method, because of the initial use of the HT, an incorrect HT envelope results in accumulated error. Yi Zhou proposed a hybrid technique combining light intensity and spectral modulation to suppress light fluctuations via a hybrid correlogram [15]. The technique mainly suppresses the instability caused by intensity fluctuations without considering other factors. Yinan Li used the HT to correct distorted interferograms with high-frequency components [16]. The authors of reference [17] used an improved version of the Teager–Kaiser energy operator (TKEO) method to remove noise and the offset component. This work mainly focused on the detection of a transparent layer. A review of the suppression methods applied in the literature indicates that the HT algorithm is the most studied approach [18]–[26]. In most methods, the HT is applied first, and errors are then corrected via a subsequent procedure. However, the HT method fails to yield stable, accurate results in the presence of noise disturbances [14]. Thus, the HT method cannot serve as an effective and accurate foundation for subsequent analysis.

To address the abovementioned problems, we present a hybrid algorithm combining two approaches: a “Gauss-type” envelope algorithm and the Carré phase correction algorithm. The basic principle of our algorithm involves the use of a “Gauss-type” curve to fit a particular part of the interference curve, enabling the envelope curve to become Gaussian-like. Thus, the envelope does not collapse, preventing the interference curve from becoming distorted. In addition, the consistency of the envelope peak position and the coherence peak position is ensured. To account for phase shift errors, the Carré algorithm (derived from PSI), which includes a self-calibration function, is chosen to address the phase problem and ensure that a precise phase is acquired. The surface topography is also reconstructed.

In addition to the details of the proposed method, a mathematical derivation is presented. The effect of chromatic dispersion is not considered. In the following, a detailed analysis based on simulations and experiments is presented. We also discuss the accuracy of the algorithm for samples with various stepwise profiles and under various conditions.

2. Theoretical Analysis

In WLPSI, an interference curve is obtained for each fixed point on the surface of the object being scanned. As the surface of the object is scanned, the curves reach their coherence peaks at different positions. The heights of various points on the surface can be distinguished by their different coherence peak positions. When the relative height (ΔH in (1)) of each point on the surface is obtained, the three-dimensional topography of the entire surface is reconstructed. Fig. 1 illustrates this concept.

$$\Delta H = N \cdot d - (\lambda/4\pi) \cdot \phi, \tag{1}$$

As shown in (1), the relative height ΔH is retrieved from two pieces of information: the first is the position information, or the location N of the coherence peak, and the second is the phase information, which is carried by the parameter ϕ. d denotes the scanning step, and λ denotes the center wavelength of the light source. As shown in Fig. 1, the surface topography is ultimately reconstructed from the height differences extracted from this position and phase information.

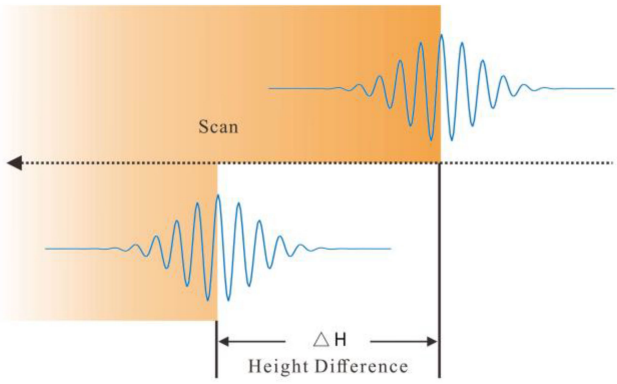

Fig. 1. Coherence peak positions during the scanning process. Peaks occur at various height positions during the scan.

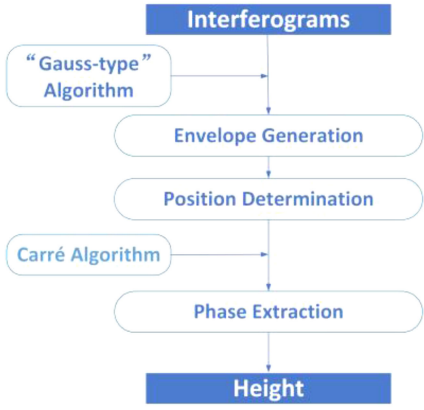

Fig. 2. Algorithm flowchart.

The proposed algorithm is divided into three parts: envelope generation, position determination, and phase extraction. The specific process is outlined in Fig. 2. The following sections describe the principles and execution of the algorithm in detail. The subsection titled "Envelope Generation" describes the principle of envelope generation and the specific implementation steps. The subsection titled "Position Determination" describes the process of fitting the continuous envelope function generated in the previous step to determine the position of the extreme point. The subsection titled "Phase Extraction" describes the process of extracting the phase based on the previous step; the height is then obtained from the extracted position and phase information.

2.1 Envelope Generation

The shape of the interference curve (as $r(\tau)$) depends on the power spectral density distribution function of the light source. The power spectral density distribution function of the light source changes, and the resulting curve shape is also different. The spectral density of the light source used by the white light interferometer is generally classified as Gaussian type or Lorentzian type; that is, due to the source spectrum, the interference fringe envelope generated by a Gaussian-type light source is Gaussian type, as shown in Fig. 3. The red dot in the figure denotes the secondary interference peak. The power spectral density distribution functions of low-pressure gas discharge lamps and light-emitting diodes (LEDs) are Gaussian type. The power density distribution function of a high-pressure gas discharge lamp is Lorentzian type.

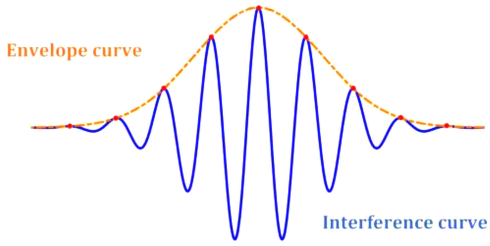

Fig. 3. Interference curve envelope.

Because of the characteristics of LEDs, such as long-life, low-cost, small-size, white light interferometry technology basically uses LEDs as interference light sources, which is precisely why the theory and experiment in this paper are based on Gaussian-type light sources. The envelope of the interference curve caused by such a light source is Gaussian type, as in (2).

$$s(\tau) = \frac{1}{\sqrt{2\pi}\sigma_s} \exp\left(-\frac{\tau^2}{2\sigma_s^2}\right), \tag{2}$$

where σ_s is the standard deviation and τ is the coordinate variable. Regardless of the noise that is present or how the shape changes, the base remains a Gaussian function, and only the base must be extracted. The new algorithm that we propose is based on this concept. We wish to use a Gaussian function to modulate the existing interference signal and then obtain the envelope. More accurately, this result is not the real envelope but rather the background shape. A Gaussian function $s(\tau)$ is selected as the template.

We use the Gaussian function $s(\tau)$ as a template to modulate the function $r(\tau)$ by convolution. After modulation, a Gaussian envelope $g(\tau)$ is acquired as the envelope of the curve. The result function $g(\tau)$ tends to be similar to the function $s(\tau)$, which has a Gauss-type shape.

The specific implementation process is as follows:

1) Suppose that the number of images acquired during a scan is m, and then the interference curve obtained for a given pixel is denoted by r(m), as shown in Fig. 4(a). We define a Gaussian template function as s(n), where n = m/4. The functions r(m) and s(n) are discrete. The sum of all elements in the function s(n) is denoted by S.
2) Data preprocessing. First, function r(m) is filtered by a zero-phase filter. The effect of this is to eliminate obvious noise terms, and the median r(m) becomes zero. The reason for using a zero-phase filter is because no offset exists for the data. Second, to prevent changes in the length of the function, zeros must be padded symmetrically on both sides of r(m).
3) In accordance with the template function g(n), the input function r(m) is modulated to obtain an envelope f(m) with the shape of a Gaussian curve. The modulation is performed via convolution, the result of which is a weighted superposition of the Gaussian function s(n) on the input function r(m), as shown in Fig. 4(b). A Gaussian function that is the same type as the source spectrum is used to extract the Gaussian contour of the input function.
4) The function g(m) obtained has the characteristics of a Gaussian function and has the same peak position as the function r(m). However, after modulation, the function g(m) does not have the same magnitude as the function r(m). For regression, g(m) is operated as in (3). The final envelope $final\_g(m)$ shown in Fig. 4(c) is obtained from (3).

$$final\_g(m) = \sqrt{\frac{g(m)}{S}}, \tag{3}$$

The advantage of the Gauss-type function obtained in this way is the uniqueness of the peak point, which helps to ensure that accurate results are obtained in the subsequent position determination step. Note that the peak position of the envelope curve is the same as that of the interference curve. The peak positions of the two functions coincide with each other, and no eccentricity exists.

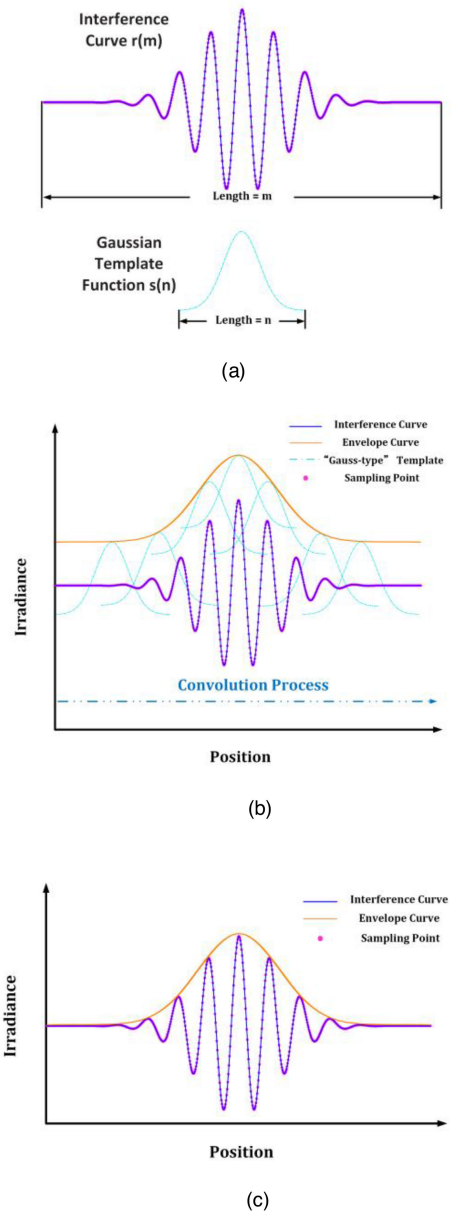

Fig. 4. Conceptual illustration of envelope generation. (a) interference curve and Gaussian template function curve; (b) convolution process; (c) magnitude correction.

Notably, the interference curve is approximated by the discrete intensity values recorded by the detector. Because the sampling is discrete, one cannot guarantee that the position of the maximum sampling intensity value is equivalent to the coherence peak position of the true interference curve. However, because the envelope generated by our algorithm is continuous and consistent, the coherence peak position of the true interference curve can be precisely estimated. This process is illustrated in Fig. 5.

2.2 Position Determination

Once the envelope ($final\_g(m)$) has been acquired, the next step is to determine the exact peak position. In practice, since the interference curve is discrete, the acquired $final\_g(m)$ is also discrete.

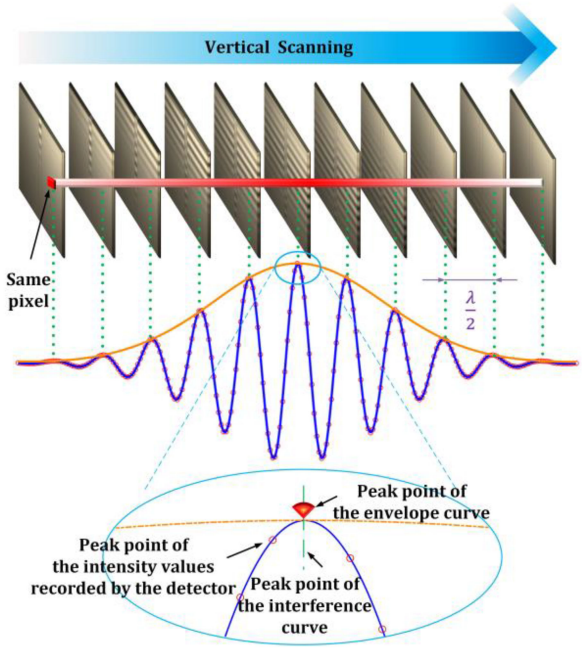

Fig. 5. Conceptual illustration of coherence peak determination.

A continuous function must be performed to fit the curve for a more accurate peak point. For this purpose, we should use a Gaussian function g(x) as shown in (4), where H, P, and W denote the height, position, and width of the Gauss peak, respectively.

$$g(x) = H \cdot \exp\left(-\left(\frac{x-P}{\frac{1}{2\cdot\sqrt{\ln 2}}\cdot W}\right)^2\right), \tag{4}$$

However, the envelope curve g(x) is an exponential function, which has high computational complexity under fitting. We attempt to alleviate this computational complexity by taking the natural logarithm of g(x), as shown in (5).

$$\ln(g) = \ln\left(H \cdot 2^{-\frac{4P^2}{W^2}+\frac{8Px}{W^2}-\frac{4x^2}{W^2}}\right), \tag{5}$$

In this way, the nonlinear relationship becomes a linear relationship.

$$\ln(g) = \ln(H) - \frac{4P^2\ln(2)}{W^2} + \frac{8Px\ln(2)}{W^2} - \frac{4x^2\ln(2)}{W^2}, \tag{6}$$

The above formula can be written in the same form as (7).

$$\ln(g) = p(x) = A + Bx + Cx^2, \tag{7}$$

Therefore, we use the least squares method as expressed in (7) to fit the center part of the envelope, calculate the specific parameters, and obtain the precise coherence peak position. After the least squares method is complete, the parameters H, P, and W of the function g(x) can be calculated from the parameters A, B, and C, as shown in (8). P is the coherence peak position, which is the parameter "N" in (1).

$$\begin{cases} H = \exp\left(A - C\cdot(B/2C)^2\right) \\ P = -B/2C \\ W = 2.35482/\sqrt{2}\cdot\sqrt{-C} \end{cases}, \tag{8}$$

2.3 Phase Extraction

In the previous step, the precise coherence peak position is acquired. The next step is to solve the parameter "ϕ" in (1). The Carré algorithm is applied, where four interferogram frames are acquired at equally spaced phase increments, as in (9).

$$\begin{cases} I_1(x,y) = I_0(x,y)\,(1+v(x,y)\cos[\phi(x,y)-3\alpha]) \\ I_2(x,y) = I_0(x,y)\,(1+v(x,y)\cos[\phi(x,y)-\alpha]) \\ I_3(x,y) = I_0(x,y)\,(1+v(x,y)\cos[\phi(x,y)+\alpha]) \\ I_4(x,y) = I_0(x,y)\,(1+v(x,y)\cos[\phi(x,y)+3\alpha]) \end{cases}, \tag{9}$$

where $v(x, y)$ is the fringe visibility and x and y are the spatial coordinates. $I_0(x, y)$ is the irradiance for a fringe-free field when the two beams are incoherent to each other. $I_1(x, y)$, $I_2(x, y)$, $I_3(x, y)$, $I_4(x, y)$ are the light intensity values corresponding to the first three frames, the first one frame, the last one frame, and the last three frames, respectively, with respect to the located peak position P.

We have the following trigonometric identity, where $I_i(x, y)$ is abbreviated as I_i (i = 0, 1, 2, 3, 4).

$$\tan(\phi(x,y)) = \frac{\{[3(I_2-I_3)-(I_1-I_4)][(I_1-I_4)+(I_2-I_3)]\}^{1/2}}{(I_2+I_3)-(I_1+I_4)}, \tag{10}$$

$\phi(x, y)$ can be resolved by (10). Then, by substituting the parameter "ϕ" into (1), the final height is obtained.

The interferograms are recorded by performing discrete vertical scanning and sampling with the phase shifter. Given that the step size of the phase shifter is d, the corresponding phase shift is $4\pi \cdot d/\lambda$. If the phase shifter has a linear error, then this error is propagated into the final reconstruction. However, Carré algorithm can eliminate this error, as shown below.

We set a reference phase shift μ with phase error ε, expressed as $\mu = \phi + \varepsilon$. Substituting μ into (10),

$$\tan^2\mu = \tan^2\phi \cdot 1, \tag{11}$$

As observed from (11), the reference phase shift is equal to the actual phase shift and is irrelevant to the phase error. Therefore, the algorithm removes the linear phase error.

3. Experimental Verification and Discussion

To verify the performance of the algorithm proposed in the previous section, experiments were conducted with two main purposes: coherence peak detection and standard samples testing. In the subsection titled "Coherence Peak Detection", we report simulations performed with the purpose of testing whether the algorithm correctly determines the locations of the coherence peaks in interference curves. The intent is to verify the feasibility of the algorithm at the micro level. In the subsection titled "Standard Sample Testing", we report experiments performed to test the height accuracy achieved with the proposed algorithm. For this purpose, the proposed algorithm was tested on different standard samples. The proposed algorithm was also compared against other algorithms under the same testing conditions. To further explore the performance of the proposed algorithm, we also performed additional experiments on scanning steps.

Two types of standard samples were used, including step samples with a height of 1.63 μm ± 10 nm and roughness samples with a roughness of 100 nm ± 10 nm. Each kind of sample has two types: one was coated with metallic silver (the normal sample), and the other was etched in thick glass (the low-reflectivity sample).

Note that here, a "favorable environment" refers to an environment with suitable isolation, a stable light source, steady readings from the phase shifter and other instruments, clear images, and a normal sample. In contrast, a "noisy environment" is an environment with mechanical vibrations, instruments exhibiting intermittent instability, an unstable light source, blurred images, and a low-reflectivity sample.

The experimental configuration was based on the Michelson interference light path configuration. The reference mirror was driven by a piezoelectric ceramic stage (PZT) from PI Co. Ltd. (P-753.2CD), and the step sample was positioned in the measurement optical path. The scan range was 14 μm, and the settling time for each scan was less than 5 ms. The scanning step distance was fixed, the center wavelength of the light source was 580 nm, and the series of interferograms for arithmetic reconstruction were recorded by a 500-megapixel camera.

3.1 Coherence Peak Detection

The model of the interference signal $I(p)$ can be expressed as (12)

$$I(p) = \int_0^{\infty} \int_0^{1} F(\beta, k, p) U(\beta) V(k) \beta d\beta dk, \tag{12}$$

Where $U(\beta)$ is the intensity distribution in the pupil plane of the objective and V(k) is the optical spectrum distribution. β is weighting factor associated with the projection angle and the diameter of the annulus of width in the pupil plane. k is angular wavenumber, p is scan position. $F(\beta, k, p)$ is represented by (13),

$$F(\beta, k, p) = O + R + 2\sqrt{OR}\cos[2\beta k(h - p) + (v - \omega)], \tag{13}$$

Where O is the effective object intensity reflectivity, R is the effective reference reflectivity, h is the height features that vary over the object surface, ω is the phase variable for the object path, and υ is the one for the reference path [27].

As can be seen from the above formula, the optical factors affecting interference can be summarized into the following six categories: ① spectral distribution of the light source; ② numerical aperture of the objective; ③ optical transmission function of system; ④ reflectivity of the tested sample and the reference mirror; ⑤ the phase difference caused by the tested sample and the reference mirror; ⑥ the step of the phase shifter (also indicated in (1)). The incorrect step caused by the environment or itself directly leads to the deviation of the final height. ②③ are the inherent parameters of the system, so $U(\beta)$ and β are considered as constants. ⑤ is hard to operate in actual experiments, ω and υ are not considered. R is regarded as a constant. Based on our previous experiments, we found that the influence of ①④⑥ on the results is more prominent and feasible to simulate, so V(k), O and p are selected as simulation variables to simulate the corresponding environment. In consideration of the Gaussian-type source spectrum, V(k) is simulated by $s(\tau)$ in (2). p has the same physical meaning as d in (2).

Therefore, the performance of the algorithm for coherence peak detection was simulated under several different conditions: 1) an ideal environment; 2) an environment with a phase shifter with an inaccurate step size or a light source with an abnormal light intensity; 3) an environment with a low-reflectivity step sample and spectral broadening source; and 4) an environment with a low-reflectivity sample, an unstable light source and blurred images with mechanical vibrations. As the environment becomes more unfavorable, the corresponding interference curves become more distorted, and the challenge of coherence peak detection increases.

Regarding coherence peak detection under ideal conditions, Fig. 6 indicates that the peak position of the envelope function coincides with that of the interference curve for a sufficiently high sampling frequency.

However, under real-world conditions, the interference curve typically exhibits a certain degree of deformation [15]. High sampling frequency brings excessive amounts of data to be stored and calculated. Therefore, compared to Fig. 6, the sampling frequency is significantly reduced during actual scanning. The reduction of sampling frequency causes the curve to exhibit a certain degree of deformation. Secondly, the interference curve is recorded with the uniform movement of the phase shifter. When the vibration exits, the phase shifter itself has hysteresis or inaccurate step size, the value that should have acquired after or before several steps is mistakenly used as the value of the current point. This case is equivalent to changing the parameter “d” in (1). In practice, the most common manifestation is spike noise, which causes the value at some point to be larger

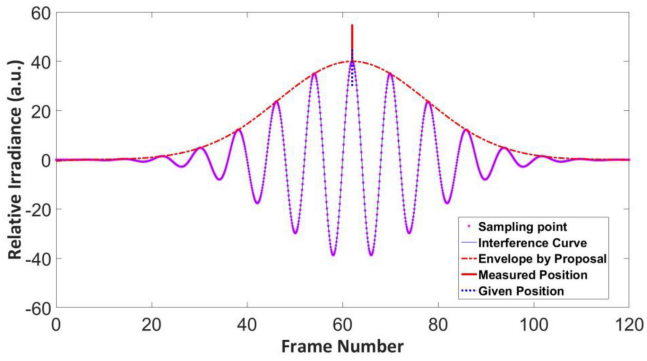

Fig. 6. Experimental results under ideal conditions.

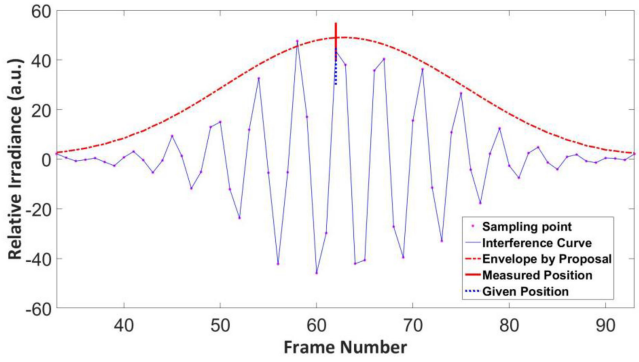

Fig. 7. Experimental results in an environment with single-frequency spike noise.

than the value at the peak point. Consequently, the location of the coherence peak is misevaluated due to spike noise.

To simulate this situation, we raise the value of the submaximal point, making it exceed the value of the peak point. A simulated interference curve with spike noise is shown in Fig. 7. The magnitude of a data point affected by spike noise exceeds the magnitude of the data point closest to the true coherence peak. However, the coherence peak position identified from the simulated curve when using the proposed algorithm is 62, indicating that the estimated envelope accurately locates the coherence peak and yields a consistent result. This result confirms that the algorithm is not affected by spike noise.

For discontinuous structures, high-frequency noise is often observed at the interface between the upper and lower surfaces. This is caused by overshoot, which causes the values of multiple secondary peaks to be higher than that of the central principal maximum, thus introducing spike noise. In this case, detection becomes more difficult when testing low-reflectivity samples, for which the fringe contrast is decreased. When the fringe contrast is low, the relative irradiance values span a narrower range, the irradiance of coherence peak and secondary peaks is close even equal. Under such circumstances, considerable errors arise when determining the location of the maximum of the curve. In the simulation, for low reflectivity, we averaged the irradiance of each peak and narrowed the integral irradiance by decreasing O; we made some secondary peaks exceed the coherence peak for overshoot; the coherent area was expanded to weaken the spectral shape by adjusting V(k). A simulated interference curve under such conditions is shown in Fig. 8. The simulated peak position is at 125, and the envelope peak position is at 124.8. Although the noise has a slight effect on the results, the peak detection performance is still acceptable.

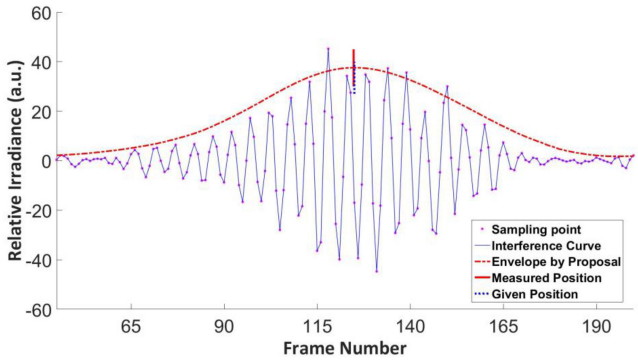

Fig. 8. Experimental result under noise conditions with low fringe contrast.

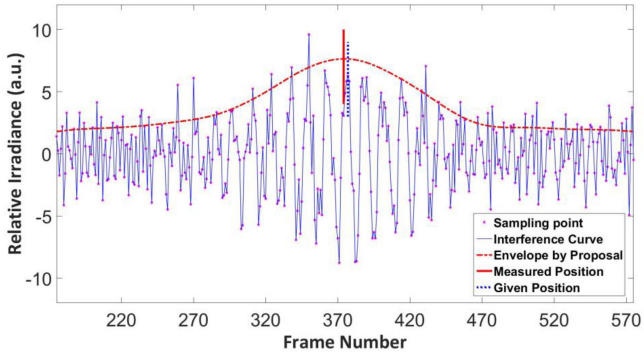

Fig. 9. Experimental result under heavy noise conditions with low reflectivity samples, blurred images and mechanical vibration.

Notably, interference curves are generated from discrete sampling points. The accuracy depends on the sampling frequency of the points used to locate the coherence peak. However, in the proposal algorithm, the accuracy depends on the continuous envelope function that is used to obtain the extremum and is not limited by the sampling frequency. Consequently, relative to the sampling point with the maximum value, the extremum of the envelope function is a more accurate estimate of the coherence peak.

Next, we consider an even more unfavorable situation in which the spectrum of the light source drifts, the images captured are blurry, and the reflectivity of the sample is low. For spectrum, we further broadened the spectrum and narrowed the irradiance to further weaken the unimodality of the curve. For image blur and vibration, random noise was added to the simulated curve. The fringe amplitude is only approximately 10 pixels in Fig. 9, whereas those in Fig. 7 and Fig. 8 are close to 80 pixels. The spectral width is close to 200 pixels. The interference signal information is buried in the noise. Under such conditions, it is an enormous challenge to achieve coherence peak detection, with most algorithms producing erroneous results. These observations also help to explain why the background noise has a strong influence on the measurement accuracy. Notably, a certain separation exists between the peak area and the noncoherent area that allows the algorithm to function. In the peak area, the first derivative of the envelope curve changes from positive to negative, and there is a unique extremum. In this case, the coherence peak position is still likely to be detected. In this example, the simulated peak position is at 377, and the envelope peak position is at 374.1. Common algorithms have little chance to detect the coherence peak at all, let alone with such a small deviation. Even in this environment, the proposed algorithm has satisfactory noise immunity.

TABLE 1
Results of Coherence Peak Detection

	1	2	3	4	5	6	7	MEAN VALUE	STANDARD DEVIATION
IDEAL	162	162	162	162	162	162	162	162	0
NOISY	162.22	162.22	161.97	162.02	162.13	162.08	162.0	162.09	0.1023

The proposed algorithm was tested under both an ideal environment and a noisy environment, with seven sets of data generated for each environment; the results are recorded in Table 1. For the normal interference curves, no location deviations occur. For the deformed interference curves, small location deviations arise. The algorithm retains satisfactory stability in a noisy environment. Even when the amplitude, contrast and shape of the interference curve are abnormal, the proposed algorithm is reasonably accurate.

3.2 Standard Sample Testing

Above, the algorithm was proven to offer high accuracy and suitable robustness in coherence peak detection. To further evaluate the performance of the algorithm, the three-dimensional reconstruction results of the algorithm were tested. The three-dimensional topography and sectional views of the algorithm under favorable and noisy environments were given. The scanning step that allows the algorithm to achieve the best effect was tested. The standard step samples and standard roughness samples were also applied to verify the validity and feasibility of the algorithm compared to those of other existing algorithms. According to this concept, this experiment is divided into three parts: self-comparison testing, optimal scanning step testing, and comparison testing.

3.2.1 Self-Comparison Testing: The following is a self-comparison of algorithm performance under different environments. The evaluation under a favorable environment was first implemented, as shown in Fig. 10.

The overall shape of the step is correctly recovered. Both the upper and lower surfaces are flat and without any tilt. The sidewalls of the step are steep, with a slight deformation on the left step edge. Little noise exists on the bottom and left upper surfaces of the step. At the junction between the sidewall and the bottom surface of the groove, some deviation is observed because of the enormous height difference. In this favorable environment, the proposed algorithm yields satisfactory results that are consistent with the actual surface of the sample.

After the instrument was moved away from the vibration isolation platform, the low-reflectivity sample was tested instead of the normal sample; the results are shown in Fig. 11. The upper and lower surfaces are still flat without any tilt, and the sidewalls are steep. By comparison with the previous results, the noise on the upper and lower surfaces is increased, particularly at the bottom of the groove. The three-dimensional map indicates that the noise is concentrated mainly in the vertical groove, which illustrates that the algorithm achieves acceptable performance in suppressing noise. The noise is small in amplitude and is straightforward to remove with a filter, which shows that the algorithm has strong robustness. Note that “repeatability” = “standard deviation” / “dean value”, reflecting the stability as a percentage. A smaller value indicates higher stability.

3.2.2 Optimal Scanning Step Testing: In the above test, the scanning step was fixed. To determine whether the scanning step affects the measurement results and further explore the performance of the algorithm, we performed additional experiments. In the same testing environment, the same sample area was tested, changing only the scanning step. With each scanning step length, seven sets of data were recorded. Due to hardware limitations, the scanning step was varied from 5 nm to 100 nm in increments of 10 nm. All obtained standard deviation data were plotted on the same graph, and the trend fit was also plotted. Based on the available data, Fig. 12 and Table 2 show that the error is smallest when the scanning step is 20 nm. After fitting the trend of the available data, we find that the point with the minimum error lies at 19 nm by searching for the extremum of the trend curve. In theory, the smaller the scanning step is, the higher the accuracy of

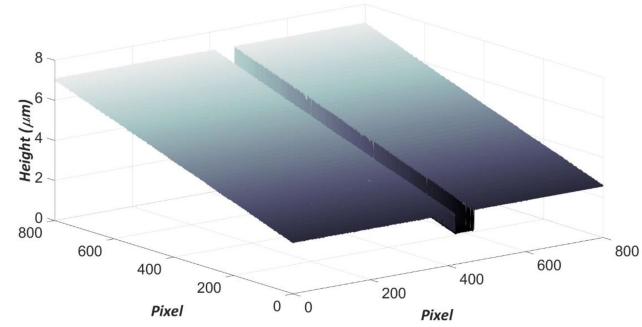

(a)

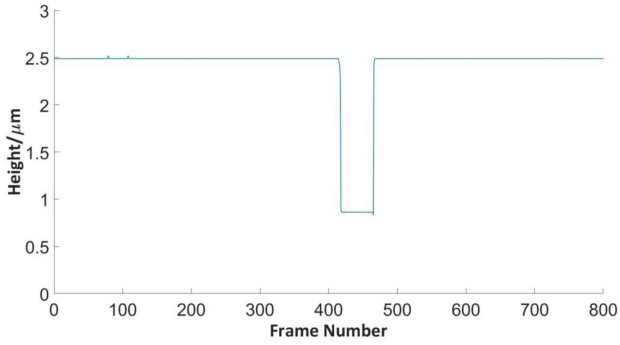

(b)

Fig. 10. Results of the normal sample in a favorable environment: (**a**) three-dimensional topography; (**b**) cross-sectional profile.

reconstruction should be. In our particular experimental environment, when the scanning step size is less than 5 nm, the noise significantly increases. When the step size is greater than 100 nm, the resolution of the surface detail decreases. When the step size is less than 5 nm, the requirements for the experimental conditions become relatively unfavorable; our experimental environment does not meet such requirements. If these requirements could be met, then smaller step sizes might yield better results. The above experimental results can serve as a reference for the selection of an appropriate scanning step.

3.2.3 Comparison Testing: After determining the optimal step under the favorable environment, the comparison test was performed under favorable and noisy environments. Standard step samples and roughness samples were selected for testing. To permit better comparisons with the previous experiment, and three previously reported algorithms were tested for comparison: the extremum algorithm, the HT algorithm and the frequency domain analysis (FDA) algorithm. In order to reflect the comparative effect more fairly, the results of the existing algorithms in the comparison testing were also obtained under the corresponding optimal scanning step. The optimal scanning step sizes of the existing algorithms were: the extremum algorithm (20 nm); the HT algorithm (55 nm); the FDA algorithm (45 nm). Consequently, the following comparison testing was performed under the condition that each algorithm reached the optimal scanning step.

The test results under different conditions, which are presented in Table 3 and Table 4, show that the proposed algorithm yields the most stable results. Compared with its performance in a favorable environment, its repeatability worsens to 0.59%; however, it is still no more than 1%, indicating that disturbances are well suppressed. The graph of standard deviation (SD) is presented to better illustrate the stability of algorithms under different environments. The standard deviations of the test values of each algorithm under different environments, and the difference between such standard

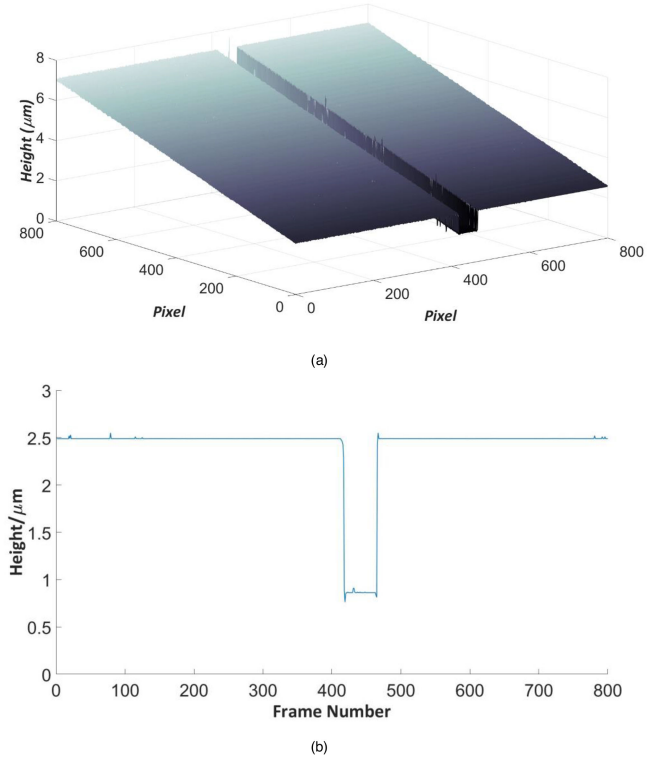

Fig. 11. Results of the low-reflectivity sample under a noisy environment: (a) three-dimensional topography; (b) cross-sectional profile.

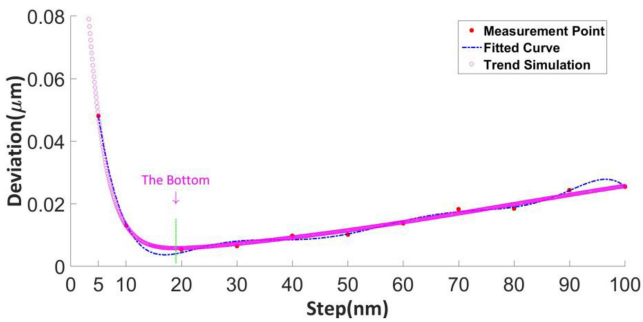

Fig. 12. Deviation results for different scanning steps.

deviations are simultaneously plotted in the same graph. In order to be able to plot both data in the same graph, double vertical axes are used. The standard deviation of height follows the "Standard Deviation" axis on the left, and the values under different environments are distinguished by curves of different colors and line types. The difference between the standard deviations of the same algorithm is represented by the stem figure, following the right "Difference" axis.

As shown in Fig. 13, the difference of the Extremum algorithm is the largest, the one of the HT algorithm is slightly higher than the one of the FDA algorithm, and the difference of the proposed algorithm is the smallest. From the stem figure, the difference of the Extremum algorithm (0.187 μm) is one order of magnitude higher than the differences of the HT algorithm (0.045 μm) and the FDA algorithm (0.029 μm), and the FDA algorithm has the best anti-noise capability in the existing algorithms. However, the difference of the proposed algorithm is 0.004 μm, which is much smaller

TABLE 2
Experimental Results For Various Scanning Steps

Trial#	Step = 5 nm	Step = 10 nm	Step = 20 nm	Step = 30 nm	Step = 40 nm	Step = 50 nm
1	1.6501	1.6208	1.6339	1.6293	1.6199	1.6326
2	1.6987	1.6412	1.6286	1.6325	1.6387	1.6229
3	1.5452	1.6271	1.6284	1.6289	1.6404	1.6379
4	1.6623	1.6433	1.6413	1.6332	1.6269	1.6196
5	1.6419	1.6185	1.6323	1.6475	1.6327	1.6203
6	1.5810	1.6090	1.6315	1.6388	1.6154	1.6227
7	1.6137	1.6086	1.6427	1.6283	1.6156	1.6035
MEAN VALUE	1.6276	1.6241	1.6341	1.6341	1.6271	1.6228
STANDARD DEVIATION	0.0479	0.0129	0.0053	0.0064	0.097	0.0100
REPEATABILITY (%)	2.95	0.79	0.32	0.39	0.59	0.62
Trial#	Step = 60 nm	Step = 70 nm	Step = 80 nm	Step = 90 nm	Step = 100 nm	
1	1.6143	1.6013	1.6133	1.600	1.6109	
2	1.6253	1.6208	1.6180	1.6024	1.5911	
3	1.6520	1.6020	1.6445	1.5811	1.6528	
4	1.6187	1.6021	1.6472	1.6433	1.6309	
5	1.6301	1.6433	1.6210	1.6129	1.5704	
6	1.6405	1.6200	1.5931	1.6481	1.5932	
7	1.6111	1.6482	1.6041	1.6432	1.6162	
MEAN VALUE	1.6274	1.6197	1.6201	1.6187	1.6094	
STANDARD DEVIATION	0.0136	0.0182	0.0183	0.0242	0.0253	
REPEATABILITY (%)	0.83	1.12	1.13	1.50	1.57	

*The unit of value that is not specifically labeled in the table is μm.

TABLE 3
Results of the Step Samples with Different Algorithms Under Favorable Environments

Trial#	Extremum	HT	FDA	Proposal
1	1.642	1.6192	1.6282	1.6339
2	1.6132	1.6197	1.6222	1.6286
3	1.6064	1.6404	1.6195	1.6284
4	1.4987	1.632	1.6179	1.6413
5	1.6023	1.6598	1.6318	1.6323
6	1.6032	1.6202	1.6392	1.6315
7	1.569	1. 6296	1.6192	1.6427
MEAN VALUE	1.5906	1.6315	1.6254	1.6341
STANDARD DEVIATION	0.0424	0.0136	0.0073	0.0053
REPEATABILITY (%)	2.66	0.83	0.45	0.32

*The unit of value that is not specifically labeled in the table is μm.

than the one of the FDA algorithm. In the comparison testing of standard step sample, the Extremum algorithm has the worst resistance to noise, while the proposed algorithm has the best stability.

After completing the test of the standard step samples, to more fully reflect the stability of the algorithm, we performed a roughness sample test. The same comparison was used. Through comparison of the data in Table 5 and Table 6 and visualization of Fig. 14, the stability of the proposed algorithm was confirmed. Fig. 14 draws the standard deviation data of roughness. Similar

TABLE 4
Results of the Step Samples with Different Algorithms Under Noisy Environments

Trial#	Extremum	HT	FDA	Proposal
1	1.655	1.6096	1.6656	1.6138
2	1.9711	1.7107	1.6323	1.6308
3	2.1007	1.7293	1.711	1.6311
4	1.3267	1.769	1.6306	1.647
5	1.698	1.6503	1.6403	1.6389
6	1.8378	1.7203	1.6243	1.625
7	1.747	1.7906	1.5801	1.6321
MEAN VALUE	1.7623	1.7114	1.6406	1.6312
STANDARD DEVIATION	0.2297	0.0586	0.0371	0.0096
REPEATABILITY (%)	13.03	3.42	2.26	0.59

*The unit of value that is not specifically labeled in the table is μm.

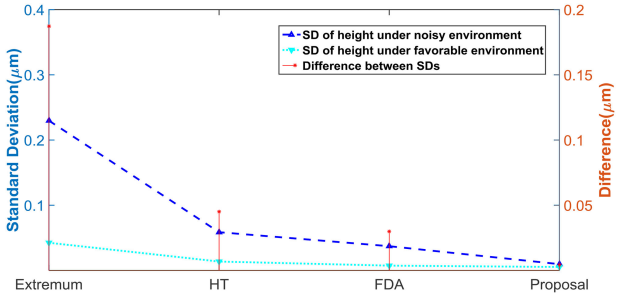

Fig. 13. Results of the step samples with different algorithms under different environments.

TABLE 5
Results of the Roughness Samples with Different Algorithms Under Favorable Environments

Trial#	Extremum	HT	FDA	Proposal
1	107.6323	105.773	105.1259	105.0841
2	108.223	105.9273	105.1347	105.7869
3	108.732	106.02843	105.4238	105.516
4	109.332	105.0284	105.2982	105.3421
5	108.4242	105.201	105.2975	105.3098
6	107.779	104.897	106.1914	105.5009
7	105.8133	105.2389	105.1142	105.0281
MEAN VALUE	107.9908	105.4420	105.3694	105.3668
STANDARD DEVIATION	1.0354	0.4236	0.3522	0.2435
REPEATABILITY (%)	0.95	0.40	0.33	0.23

*The unit of value that is not specifically labeled in the table is nm.

to Fig. 13, the standard deviation of roughness follows the “Standard Deviation” axis on the left, the right “Difference” axis is appropriate for the difference between the standard deviations of the same algorithm. As the stem figure shown, the basic trend of the data is consistent with Figure 13. The Extremum algorithm has the largest difference (10.93 nm) and is much higher than other algorithms. The difference of the HT algorithm (3.45 nm) is twice the one of the FDA algorithm (1,49 nm), while the difference of the proposed algorithm (0.44 nm) is only one-third of the one of the FDA algorithm. The repeatability of the proposed algorithm is better than 1%. In the comparison testing of standard roughness sample, the stability of the proposed algorithm is still optimal.

From the test results of the standard step sample and the roughness sample, the proposed algorithm is superior to the existing algorithms. The Extreme algorithm is done by searching the maximum value. The spike noise that causes the value at some point to be larger than the value at the

TABLE 6
Results of the Roughness Sample with Different Algorithms Under Noisy Environments

Trial#	Extremum	HT	FDA	Proposal
1	115.3478	108.3625	107.6381	105.2394
2	124.0987	109.3189	104.0999	105.1392
3	120.039	111.655	106.5876	106.2901
4	104.2089	107.7414	105.9813	106.2395
5	134.7931	119.3025	110.7197	107.2387
6	101.537	111.1137	106.8532	106.6205
7	132.789	106.9375	106.8864	106.4129
MEAN VALUE	118.9734	110.6331	106.9666	106.1686
STANDARD DEVIATION	11.9743	3.8791	1.8473	0.6919
REPEATABILITY (%)	10.06	3.50	1.72	0.65

*The unit of value that is not specifically labeled in the table is nm.

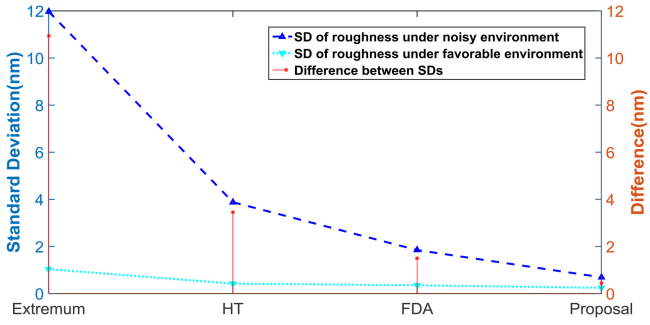

Fig. 14. Results of the roughness samples for different algorithms under different environments.

peak point makes the Extreme algorithm misjudge the peak position. The HT algorithm generates an envelope based on the magnitude of intensity. Any change in amplitude affects the envelope, which ultimately leads to false positives. In addition, the HT algorithm has a premise that the background light intensity has to be constant. However, during the actual scanning process, this condition is not always satisfied as the position of the interference objective changes. The FDA algorithm solves the surface height by the slope of the line at the angular wavenumber. The accuracy depends on the linearity of the phase and the fitting error. Also, the group velocity refractive index needs to be considered. The conditions of the noisy environment affect the linearity of the phase and the group velocity refractive index. The proposed algorithm in this paper is to generate the envelope curve by using the spectral function (Gaussian function) of the light source as a template function. The Gaussian-type envelope has the unimodal nature. Moreover, its accuracy is not limited to the sampling frequency. For amplitude changes caused by spike noise and changes of the background light intensity, the envelope does not deform. The noisy environment does not cause a fundamental change in the shape of the spectrum, so the algorithm has a stable performance under both conditions.

4. Conclusions

We developed a new surface morphology algorithm for use in WLPSI profilers that combines a "Gauss-type" envelope algorithm with the Carré phase algorithm. Detailed mathematical derivations and experimental verifications were conducted. From the two perspectives of coherence peak detection (the most critical part of any WLPSI recovery algorithm) and three-dimensional sample surface morphology reconstruction, in both a favorable environment and a noisy environment, the effectiveness of the proposed algorithm was verified. It is demonstrated that the best results are achieved when the scanning step is between 15 and 20 nm. In the favorable environment, the

best repeatability was 0.32% for the measured step height and 0.23% for roughness; these values increased to 0.59% and 0.65%, respectively, in the noisy environment. For the 1.63-μm step sample, the SD of the results increased by no more than 0.005 μm. For the 100-nm roughness sample, the SD did not exceed 0.5 nm. These results show that the algorithm can effectively suppress disturbances and exhibits strong robustness and stable repeatability.

In the proposed algorithm, the effect of chromatic dispersion is not considered. This algorithm is only applicable to a Gaussian spectrum. Moreover, the algorithm does not perform well in suppressing nonlinear errors. Because of experimental limitations, no research involving chromatic dispersion or nonlinear errors was conducted. Under favorable conditions, poor-quality interference curves do not appear. When a problem exists with the experimental configuration, better measurement results can be achieved using the proposed algorithm. However, the compensation provided by the algorithm can generally reduce the instrument dependence on the environment. Building a high-quality test environment comes at a high cost. Through the use of the proposed algorithm for performance enhancement, the cost of WLPSI instrumentation can be somewhat reduced, thereby broadening its range of application.

References

[1] Y. Arieli, S. Epshtein, and I. Yakubov, "Surface measurements by white light spatial-phase-shift imaging interferometry," *Appl. Opt.*, vol. 22, no. 13, pp. 15632–15638, Jun. 2014.

[2] T. Guo, L. Ma, and J. Chen, "Microelectromechanical system surface characterization based on white light phase shifting interferometry," *Opt. Eng.*, vol. 50, no. 5, pp. 053606-1–053606-7, May 2011.

[3] L. Deck and P. D. Groot, "High-speed noncontact profiler based on scanning white-light interferometry," *Appl. Opt.*, vol. 33, no. 31, pp. 7334–7338, Nov. 1994.

[4] Y. S. Ghim and A. Davies, "Complete fringe order determination in scanning white-light interferometry using a Fourier-based technique," *Appl. Opt.*, vol. 51, no. 12, pp. 1922–1928, Apr. 2012.

[5] J. Schmit and A. Olszak, "High-precision shape measurement by white-light interferometry with real-time scanner error correction," *Appl. Opt.*, vol. 41, no. 28, pp. 5943–5950, Oct. 2002.

[6] H. Muhamedsalih, F. Gao, and X. Jiang, "Comparison study of algorithms and accuracy in the wavelength scanning interferometry," *Appl. Opt.*, vol. 51, no. 36, pp. 8854–8862, Dec. 2012.

[7] J. H. Kim, S. W. Yoon, and L. Jeong-Ho, "New algorithm of white-light phase shifting interferometry pursing higher repeatability by using numerical phase error correction schemes of pre-processor, main processor, and post-processor," *Opt. Lasers Eng.*, vol. 46, no. 2, pp. 140–148, Aug. 2008.

[8] S. R. Kim, J. H. Kim, and H. J. Pahk, "Fringe-order determination method in white-light phase-shifting interferometry for the compensation of the phase delay and the suppression of excessive phase unwrapping," *J. Opt. Soc. Korea*, vol. 17, no. 5, pp. 415–422, Oct. 2013.

[9] S. Ma, C. Quan, and R. Zhu, "Surface profile measurement in white-light scanning interferometry using a three-chip color CCD," *Appl. Opt.*, vol. 50, no. 15, pp. 2246–2254, May 2011.

[10] S. Ma, C. Quan, and R. Zhu, "Application of least-square estimation in white-light scanning interferometry," *Opt. Lasers Eng.*, vol. 49, no. 7, pp. 1012–1018, Jan. 2011.

[11] Z. Lei, X. Liu, and L. Chen, "A novel surface recovery algorithm in white light interferometry," *Meas.*, vol. 80, pp. 1–11, Dec. 2016.

[12] P. Pavliček and V. Michálek, "White-light interferometry-envelope detection by Hilbert transform and influence of noise," *Opt. Lasers Eng.*, vol. 50, no. 8, pp. 1063–1068, Mar. 2012.

[13] Q. Wang, "Random errors for the measurement of central positions in white-light interferometry with the least-squares method," *J. Opt. Soc. America A*, vol. 32, no. 8, pp. 1536–1543, Aug. 2015.

[14] P. Pavliček, V. Svak, and I. Yakubov, "Noise properties of Hilbert transform evaluation," *Meas. Sci. Technol.*, vol. 26, pp. 085207/1–085207/9, Jul. 2016.

[15] Y. Zhou, Y. Tang, and J. Zhu, "Characterization of micro structure through hybrid interference and phase determination in broadband light interferometry," *Appl. Opt.*, vol. 58, no. 8, pp. 2301–2306, Mar. 2017.

[16] Y. Li, M. Kastner, and E. Reithmeier, "Vibration-insensitive low coherence interferometer (LCI) for the measurement of technical surfaces," *Meas.*, vol. 104, pp. 36–42, Mar. 2017.

[17] G. Gianto, F. Salzenstein, and P. Montgomery, "Comparison of envelope detection techniques in coherence scanning interferometry," *Appl. Opt.*, vol. 55, no. 24, pp. 6763–6774, Aug. 2016.

[18] P. K. Upputuri, H. F. Wang, and N. K. Mohan, "White light Interferometry for surface profiling with colour CCD," *Opt. Lasers Eng.*, vol. 50, pp. 1084–1088, Feb. 2012.

[19] L. M. Manojlovic and M. B. Zivanov, "Spectrally resolved white-light interferometric sensor for absolute position measurement based on hilbert transform," *IEEE Sensors J.*, vol. 12, no. 6, pp. 2199–2204, Jun. 2012.

[20] Z. Guo, H. Zhang, and X Chen, "Influence of vibration disturbance during polarization coupling measurement of polarization-maintaining fiber," *Appl. Opt.*, vol. 50, no. 20, pp. 3553–3558, Jul. 2011.

[21] M. Roy, I. Copper, and P. Moore, "White-light interference microscopy: Effects of multiple reflections within a surface film," *Opt. Exp.*, vol. 13, no. 1, pp. 164–170, Jan. 2005.

[22] K. G. Larkin, "Efficient nonlinear algorithm for envelope detection in white light interferometry," *J. Opt. Soc. America A*, vol. 13, no. 4, pp. 832–843, Apr. 1996.
[23] P. K. Upputuri, L. Gong, and H. Wang, "Measurement of large discontinuities using single white light interferogram," *Opt. Exp.*, vol. 22, no. 22, pp. 27373–27380, Nov. 2014.
[24] J. Liu, J. Tan, and C. Zhao, "Phase-shift resolving confocal microscopy with high axial resolution, wide range and reflectance disturbance resistibility," *Opt. Exp.*, vol. 17, no. 18, pp. 16281–16290, Aug. 2009.
[25] W. Xie, P. Lehmann, and J. Niehues, "Signal modeling in low coherence interference microscopy on example of rectangular grating," *Opt. Exp.*, vol. 24, no. 13, pp. 14283–14300, Jun. 2016.
[26] Z. Xu, V. Shilpiekandula, and K. Youcef-toumi, "White-light scanning interferometer for absolute nano-scale gap thickness measurement," *Opt. Exp.*, vol. 17, no. 17, pp. 15104–15117, Aug. 2009.
[27] X. C. D. Lega and P. D. Groot, "Signal modeling for low-coherence height-scanning interference microscopy," *Appl. Opt.*, vol. 43, no. 25, pp. 4821–4831, Sep. 2004.